applied sciences

MDPI

Article

State–Space Modelling and Stability Analysis of Solid-State Transformers for Resilient Distribution Systems

Dillip Kumar Mishra [1,*], Mohammad Hossein Abbasi [1], Mohsen Eskandari [2], Saroj Paudel [1], Sourav K. Sahu [3], Jiangfeng Zhang [1] and Li Li [4]

[1] Department of Automotive Engineering, Clemson University, Clemson, SC 29607, USA
[2] School of Electrical Engineering and Telecommunication, University of New South Wales, Sydney, NSW 2052, Australia; m.eskandari@unsw.edu.au
[3] School of Electrical Engineering, BIT Mesra, Mesra 835215, India
[4] School of Electrical and Data Engineering, University of Technology Sydney, Sydney, NSW 2007, Australia
* Correspondence: dillipkumarmishra4@gmail.com

Abstract: Power grids are currently undergoing a significant transition to enhance operational resilience and elevate power quality issues, aiming to achieve universal access to electricity. In the last few decades, the energy sector has witnessed substantial shifts toward modernizing distribution systems by integrating innovative technologies. Among the innovations, the solid-state transformer (SST) is referred to as a promising technology due to its flexible power control (better reliability) and high efficacy (by decreasing losses) compared with traditional transformers. The design of SST has combined three-stage converters, i.e., the input, isolation, and output stages. The key objective of this design is to implement a modern power distribution system to make it a more intelligent and reliable device in practice. As the power converters are used in SST, they exhibit non-linear behavior and can introduce high-frequency components, making stability more challenging for the system. Besides, the stability issue can be even more complicated by integrating the distributed energy resources into the distribution system. Thus, the stability of SST must be measured prior to /during the design. To determine stability, state-space modeling, and its controller design are important, which this paper explains in detail. Indeed, the system's stability is measured through the controllability and observability test. Further, the stability analysis is performed using frequency and time-domain diagrams: the Bode plot, Nyquist plot, Nichols chart, Root locus, pole-zero plot, and Eigen plot. Finally, the SST Simulink model is tested and validated through real-time digital simulation using the OPALRT simulator to show its effectiveness and applicability. The stability performance of the proposed SST is evaluated and shows the effectiveness of the controller design of each converter circuit.

Keywords: solid-state transformer; smart grid; stability analysis; state–space model; resilience

Citation: Mishra, D.K.; Abbasi, M.H.; Eskandari, M.; Paudel, S.; Sahu, S.K.; Zhang, J.; Li, L. State–Space Modelling and Stability Analysis of Solid-State Transformers for Resilient Distribution Systems. *Appl. Sci.* **2024**, *14*, 1915. https://doi.org/10.3390/app14051915

Academic Editor: Manuela Sechilariu

Received: 21 December 2023
Revised: 19 February 2024
Accepted: 20 February 2024
Published: 26 February 2024

1. Introduction

Over the past few decades, extreme events such as natural disasters, cyber-attacks, power system equipment failures, and power thefts have increased, eventually impacting the power system infrastructure, including distribution systems [1]. Consequently, a power system blackout may occur, affecting people's social and economic life [2]. As traditional power system networks are large ring systems, an extreme event may affect many loads and components [3]. However, much research has been carried out in the area of power system migration, where the main aim was to convert from bulk power networks to small-scale networks [4,5]. The small-scale networks have been established through the development of renewable energies (RESs) and their integration into bulk power networks [6], for example, microgrids (MGs) and smart grids (SGs). These are generally connected to the bulk power system, making them a grid-connected mode [7,8]. Further, it can change to the islanded

mode while in events to avoid corresponding impacts on the distribution system and supply the local loads [9]. Furthermore, the deployment of MGs and SGs including electric vehicles can enhance system reliability and resiliency of the power distribution system in responding to extreme operating conditions [10,11].

As noted, it has been seen that the integration of RESs has increased during the past few decades, which plays a crucial role in the distribution systems for grid modernization [12]. However, due to the intermittency of the RESs, it has certain challenges, which make the system complex and unstable. The most noticeable challenge is uncertainty, which means it depends on environmental factors such as solar insolation and wind speed for solar and wind systems, respectively [13]. To deal with these challenges, the advanced power electronics in distribution systems play a crucial role in regard to the control of power (both active and reactive power) flow to enable DC-operated technology [14], protection [15], mitigating the power quality issues, and reducing harmonics. To address these benefits, power electronics are reconfigured in a different way to make it possible for the determination of power quality problems [16]. It is critical for the distribution networks that the reliability factor is always a prime concern. With this objective, using a modern power electronics device, a solid-state device is pronounced, named the SST. SST is treated as an evolving technology for providing power supply to the consumer through MGs or SGs [17]. Besides, the SST is a high-frequency transformer with a power electronic converter and is an alternative to the traditional bulky and non-smart transformer.

In the past decades, researchers have shown interest in modeling and the development of SST for MG and SG applications. In [18,19], the design and response of SSTs are addressed through their converter stages and controllers. In [20], average models and their controllers are proposed and explored through descriptive simulation studies. Further, in [21], the stability aspect of SST and validation, which has been done through the distribution system, is presented. In this regard, many motivating test models of transient instabilities have been developed, and their importance to the link topologies of SSTs in various operating regions is demonstrated [22]. The most prominent manufacturers of SST, namely, ABB, ETH Zurich, EPRI, Siemens, and FREEDM Systems Center, have conducted cutting-edge research to upgrade the conventional transformer to an intelligent one. They have designed and tested various topologies to improve the performance and facilities of SST to the connected devices [23–25]. In [26], the FREEDM Systems Center is presented with a start-up SST structure named Generation-1-SST, which can be used in medium-voltage-based MG. Further development has been done with a multi-cell-based DC-DC converter for SST, which is proposed in [27]. In [28], the stability of the SST has been studied with different control methods by incorporating renewable energy resources. Middlebrook's criterion is used to check the stability. In [29], small-signal stability of SST is studied using a dynamic phasor-based model. Darshit et al. [21] analyzed the SST stability on account of harmonic resonance in the distribution system. Extending to the study on [21], the modified source impedance-based stability criterion has been proposed [30]. The stability analysis considers a Z+Z type cascade system, an impedance analysis in SST explained in [31]. However, the research on SST stability is lacking in the literature and must be considered a vital factor. Thus, the stability aspect of each stage (input, isolation, and output) of the SST needs to be emphasized, which this paper addresses.

This study develops a state–space and a transfer-function-based model with a proper SST controller to reduce system complexity and cost. The state–space parameters (A, B, C, and D) of the converter's input, isolation, and output stages are estimated. Each converter stage has its own controller and filter circuit. The PI controller is implemented in this design due to its simplicity, robustness, and excellent control action. The transfer function model of each converter is derived from the state–space model. By using the transfer function equation, the stability of the proposed design is tested in terms of frequency response, time response, controllability, and observability. Furthermore, the Simulink design of the proposed system is established in MATLAB, and the controller is designed through MATLAB SISOTOOL. The state–space model is designed for the stability study

with and without a controller. In the proposed methodology, the user can simply design the controller part from the unstable model through MATLAB SISOTOOL, thereby making the system robust and stable. Thus, researchers can easily measure the system's stability, sensitivity, controllability, and observability.

This article is organized as follows. Section 1 provides an introduction to SST and a literature review. Section 2 outlines the fundamentals and different types of SST topology. In Section 3, the continuous-time average state–space model and its transfer function model are formulated. This section categorizes the converter stage into the input, isolation, and output stages with the state–space model. Finally, the result and discussion parts of the proposed model are provided in Section 4, followed by the conclusions in Section 5.

The main contribution of the paper is summarized as follows:

- The state-space model of each converter is derived.
- The stability of converters has been analyzed by integrating it with additional control methods.
- Time-domain and frequency-domain performance have been shown to measure the system's stability.
- The proposed model has been simulated and validated using an OPAL-RT real-time digital simulator.

2. Fundamental Topologies of SST

Various architectures are available for each of the three stages of SST. The topology is determined depending on the application of SST. The different types of topologies are Type-A (A-1 and A-2), Type-B, Type-C, Type-D, and Type-E [32]. This study adopts the Type-D-based SST topology [33] because it has numerous advantages, such as DC connectivity, fault isolation, proper voltage regulation, easy integration with RESs and storage, and volt-ampere reactive (VAR) compensation. In the design, the architecture for each stage should be chosen appropriately, and the problems should be addressed by integrating them into a single system to deliver regulated voltage at each stage.

The fundamental three-stage architecture of SST is presented in Figure 1. The detailed input, output, and other critical parameters can be seen in Appendix A. The input stage, which is also called the AC–DC stage, contains a single-phase AC–DC IGBT-based converter that operates at a high switching frequency. The isolation stage, which is also called the DC-DC stage, comprises two H-bridges with a high-frequency transformer. A DAB converter is also applied in this stage [34]. The output of the input stage is fed to the DAB converter, and the output of the converter is fed to the inverter or is considered the output stage. In the output stage, a filter circuit is added to mitigate the voltage and power quality issues. The output stage is usually supplied to low-voltage user applications.

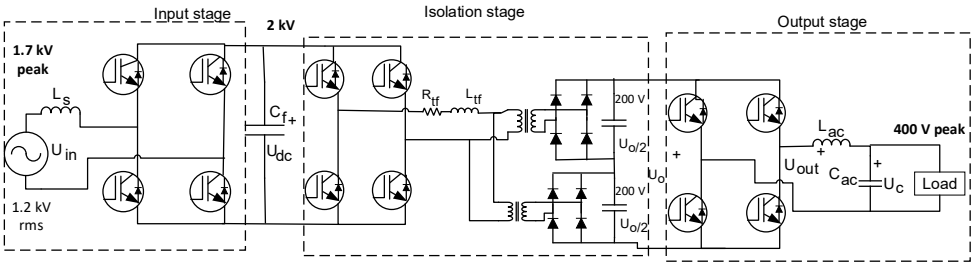

Figure 1. Three-stage SST architecture.

3. Continuous-Time Average State–Space Model

In this section, the design of the state–space model and the continuous-time transfer function model is formulated. The controller of each stage is derived to enhance system stability and performance. Furthermore, the different parameters are calculated and presented in tables to determine the stability, frequency level range, and DC gain of each stage.

3.1. Input Stage (AC-DC)

Formulation: The input stage of the SST is the conversion of AC to DC signal, shown as architecture and equivalent diagram in Figures 2a and 2b, respectively. Equations (1) and (2) represent the input voltage; however, in Equation (2), the duty cycle is taken as an average over a switching time. Referred to Figure 2b, Equation (3) is formed by applying the KVL equation. Further, considering changes as a minute value in the DC signal, Equation (3) can be modified as Equation (4). Equation (5) is solved by subtracting Equation (3) from Equation (4). Thereafter, by applying Laplace transform to Equation (5), Equation (6) and its updated version in Equation (7) are obtained, which represent the open-loop transfer function of the input stage with the inductor current.

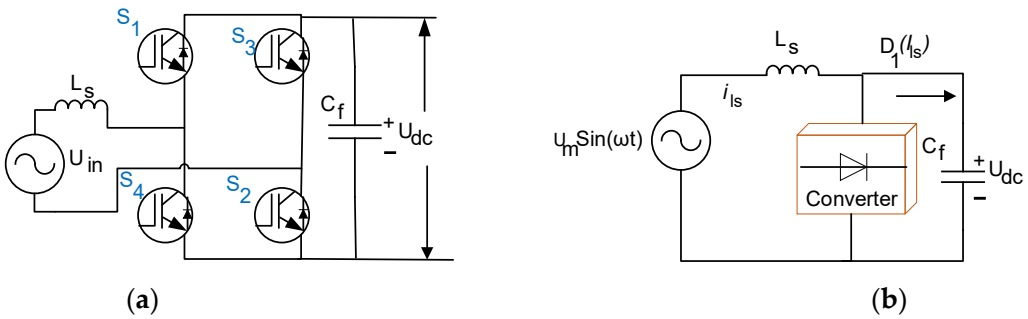

Figure 2. (**a**) AC-DC stage architecture, (**b**) Equivalent diagram of AC–DC stage.

Further, the transfer function of the input stage through DC-link capacitance current is presented in Equation (8). Similarly, Equations (9)–(11) are solved to reach Equation (12), which represents the ratio of the change in output DC link voltage to any change in input current.

$$U_s(t) = U_{dc}\mathbb{D} = K_m \sin(\omega t) U_{dc} \tag{1}$$

$$U_s(t) = U_{dc}\mathbb{D}_1(t) = U_m \sin(\omega t) \tag{2}$$

$$U_m \sin(\omega t) - U_{dc}\mathbb{D}_1(t) = L_f \frac{d(i_{ls}(t))}{dt} \tag{3}$$

$$U_m \sin(\omega t) - U_{dc}(\mathbb{D}_1 + \triangle\mathbb{D}_1)(t) = L_f \frac{d(i_{ls} + \triangle i_{ls}(t))}{dt} \tag{4}$$

$$-\triangle\,\mathbb{D}_1(t) U_{dc} = L_f \frac{d\triangle\, i_{ls}}{dt} \tag{5}$$

$$-\triangle\,\mathbb{D}_1(s) U_{dc} = sL_s \triangle\, i_{ls}(s) \tag{6}$$

$$\frac{\triangle i_{ls}(s)}{\triangle D_1(s)} = \frac{-U_{dc}}{sL_s} = G_{in} \tag{7}$$

$$C_f \frac{dU_{dc}(t)}{dt} = \mathbb{D}_1(i_{ls}(t)) \tag{8}$$

$$C_f \frac{d(U_{dc}(t) + \triangle U_{dc}(t))}{dt} = \mathbb{D}_1((i_{ls}(t) + \triangle i_{ls}(t))) \tag{9}$$

$$\frac{d(\triangle U_{dc}(t))}{dt} = \frac{1}{C_f}\mathbb{D}_1(\triangle i_{ls}(t)) \tag{10}$$

$$s\triangle U_{dc}(s) = \frac{1}{C_f}\mathbb{D}_1(\triangle i_{ls}(t)) \tag{11}$$

$$\frac{\triangle U_{dc}(s)}{\triangle i_{ls}(t)} = \frac{\mathbb{D}_1}{sC_f} = G_{vi} \tag{12}$$

State–Space Model: Furthermore, the state–space model presented in Equations (13) and (14) denotes the state and output equation of the system where A, B, C, and D are the state, control, output, and transmission matrices, respectively. The overall transfer function of the input stage has been derived, and the state–space parameters are measured in the results section. Here x is the state variable, which is: inductor current (i_{ls}) and capacitor voltage (U_{dc}) and u is the input as U_{ref}.

$$\dot{x} = Ax + Bu \tag{13}$$

$$y = Cx + Du \tag{14}$$

Considering the input stage transfer function as derived in (7) and (12), two controllers have been designed using MATLAB SISOTOOL, as per Figure 3. Thus, corresponding to G_{vi} and G_{in}, the PI controllers are G_{PI1} and G_{PI2}, respectively.

$$G_{PI1} = \frac{-3.82 \times 10^{-6}s + 6.5 \times 10^{-6}}{s}$$

$$G_{PI2} = \frac{-2.7 \times 10^{-6}s + 259.2 \times 10^{-6}}{s}$$

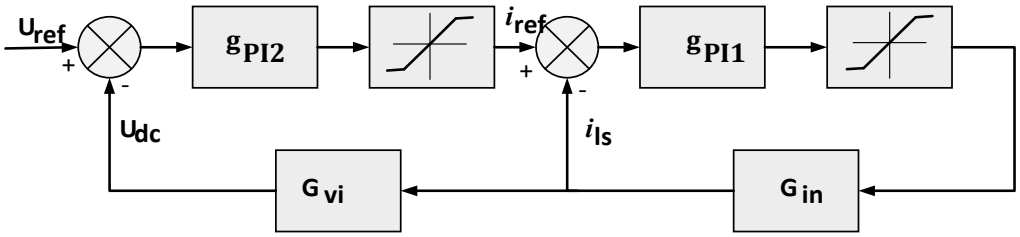

Figure 3. Control block representation of input stage.

3.2. Isolation Stage (DC-DC)

In this stage, the DAB converter is considered for DC-DC conversion. A high-frequency transformer is placed between DAB, as depicted in Figure 4a, and the equivalent diagram is depicted in Figure 4b. The DAB converter deals with three main parameters, namely, phase shift between two bridges (Ø), duty cycle ratios (𝔻), and switching frequency (fs). The other parameters are as follows: R_{tf} represents the equivalent of winding resistance and switching on resistance; L_{tf} is the leakage inductance of the transformer. The leakage inductance is calculated using Equation (20). Refer to Equation (15), the variation in transformer output with different frequencies and leakage inductance is shown in Figure 5.

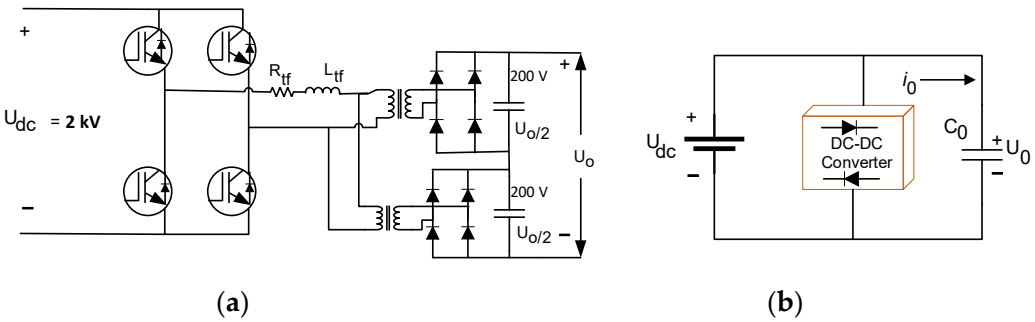

Figure 4. (**a**) DC-DC stage architecture, (**b**) Equivalent diagram of DC-DC stage.

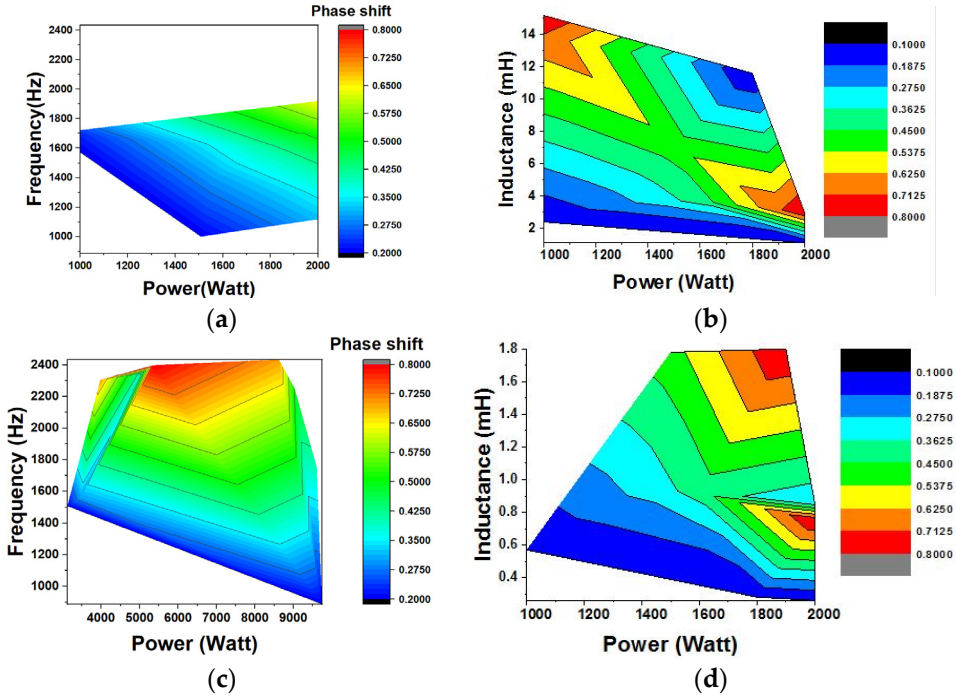

Figure 5. Inductance versus (**a**) frequency with a phase shift of 400 V, (**b**) power with a phase shift of 400 V (**c**) frequency with a phase shift of 200 V, (**d**) power with a phase shift of 200 V.

Moreover, the duty cycle ratio of the proposed scheme is fixed to 0.5. Subsequently, the phase shift modulation technique is used here to control the operation of DAB. The transferred power from one stage of DAB to the other stage can be expressed in Equation (16). Further, the state–space model of the DAB can be formulated as Equation (17) by assuming the two-state variables of the proposed systems, namely, the current through the inductor (i_L) and the voltage across the capacitor (U_0). Equations (17) and (18) are time-variant and nonlinear. To ensure that the system is time-invariant and linear, the traditional state–space averaging procedure is applied to characterize a state variable x(t) by utilizing its Fourier series expansion as given in Equation (19). To make a simple analysis, we have considered the simple full bridge converter circuit in the output side of the transformer with a single DC link. When the Fourier analysis is applied in Equations (17) and (18), Equations (20)–(25) are obtained. In this Fourier analysis, only the 0th and 1st-order terms are considered, while other higher-order terms of state variables are neglected.

$$P = \frac{U^2}{2 \times \pi \times f \times L} \varnothing \left(1 - \frac{\varnothing}{\pi}\right) \tag{15}$$

$$P_{DAB} = \frac{U_{dc} U_0}{2 N f_s L_{tf}} \mathbb{D}(1 - \mathbb{D}) \tag{16}$$

$$\text{here, } L_{tf} = \frac{L_1}{N^2} + L_2$$

$$\frac{di_L(t)}{dt} = -\frac{R_{tf}}{L_{tf}} i_L(t) + \frac{T_1(t)}{L_{tf}} U_{dc}(t) - \frac{T_3(t)}{L_{tf}} U_0(t) \tag{17}$$

$$\frac{dU(t)}{dt} = -\frac{1}{RC_0} U(t) + \frac{T_2(t)}{C_0} i_L(t) - \frac{I_0}{C_0} \tag{18}$$

$$X(t) = \sum_{k=\infty}^{\infty} X_k(t) e^{jk\omega t} \tag{19}$$

where ω =2πf and $X_k(t)$ is the k^{th} coefficient in the Fourier series analysis.

$$\frac{d\,U_o^0}{dt} = -\frac{d\,i_o^0}{C_0} - \frac{U_o^0}{RC_0} + \frac{T_2^0}{C_0} i_L^o + \frac{2T_2^{1real}}{C_0} i_L^{1real} + \frac{2T_2^{1imag}}{C_0} i_L^{1imag} \quad (20)$$

$$\frac{d\,U_o^{1real}}{dt} = -\frac{i_o^{1real}}{C_0} - \frac{U_o^{1real}}{RC_0} - \omega U_o^{1imag} + \frac{T_2^0}{C_0} i_L^{1real} + \frac{T_2^{1real}}{C_0} i_L^0 \quad (21)$$

$$\frac{d\,U_o^{1imag}}{dt} = -\frac{i_o^{1imag}}{C_0} - \frac{U_o^{1imag}}{RC_0} - \omega U_o^{1real} + \frac{T_2^0}{C_0} i_L^{1imag} + \frac{T_2^{1imag}}{C_0} i_L^0 \quad (22)$$

$$\frac{d\,i_L^0}{dt} = -\frac{R_{tf}}{L_{tf}} i_L^0 + \frac{1}{L_{tf}} U_{dc}^0 T_1^0 + \frac{2T_1^{real}}{L_{tf}} U_{dc}^{1real} + \frac{2T_1^{1imag}}{L_{tf}} U_{dc}^{1imag} - \frac{1}{L_{tf}} U_{oc}^0 T_2^0 + \frac{2T_2^{real}}{L_{tf}} U_o^{1real} + \frac{2T_2^{1imag}}{L_{tf}} U_o^{1imag} \quad (23)$$

$$\frac{d\,i_L^{1real}}{dt} = -\frac{R_{tf}}{L_{tf}} i_L^{real} + \omega i_L^{1imag} + \frac{U_{dc}^{real}}{L_{tf}} T_1^0 + T_1^{1real} U_{dc}^0 - \frac{T_2^0}{L_{tf}} U_o^{1real} + T_2^{1real} U_o^0 \quad (24)$$

$$\frac{d\,i_L^{1imag}}{dt} = -\frac{R_{tf}}{L_{tf}} i_L^{imag} + \omega i_L^{1real} + \frac{U_{dc}^{imag}}{L_{tf}} T_1^0 + T_1^{1imag} U_{dc}^0 - \frac{T_2^0}{L_{tf}} U_o^{1imag} + T_2^{1imag} U_o^0 \quad (25)$$

The transient behavior of the DAB converter in terms of voltage variations is considerably slower in the input than in the output. Therefore, the 0th term of input voltage is $U_{dc}^0 = U_{dc}$ and $i_o^0 = i_0$. The transient behavior of the first term of input voltage and load current is neglected, which are U_{1real} and i_{1real}. In this design, the converters are operating in 50% of the duty cycle. Thus, the first-order terms of T_1 (t) and T_2 (t) are similar to zero order and are presented in Equations (26)–(29). Moreover, in Equations (17) and (18), the independent state variables are the inductor current and capacitor voltage, which form the state–space model of the DAB converter with the state vector x(t) and the control vector u(t). Further, Equations (30) and (31) represent the state–space model with the input and output signals of the DAB converter. Therefore, the model parameters are input voltage source (U_{dc}), inductor current (i_L), and duty cycle ($\mathbb{D}$). When T_1^{1imag} and T_1^{1real} are introduced into Equations (20) and (25), the state–space model becomes Equation (31). Furthermore, the zero initial states are assumed in Equation (32), which are, i_L^0, U_o^{1real}, U_o^{1imag} are similar to zero order, and Equation (32) becomes Equation (33).

$$T_1^{1imag} = -\frac{2}{\pi} \quad (26)$$

$$T_1^{1real} = 0 \quad (27)$$

$$T_2^{1imag} = -\frac{2\cos\mathbb{D}\pi}{\pi} \quad (28)$$

$$T_2^{1real} = -\frac{2\sin\mathbb{D}\pi}{\pi} \quad (29)$$

$$\frac{X(t)}{dt} = A_1 x(t) + B_1 u(t) \quad (30)$$

$$Y(t) = C_1 x(t) + D_1 u(t) \quad (31)$$

$$\frac{d}{dt}\begin{bmatrix} \triangle U_o \\ \triangle i_L^{1real} \\ \triangle i_L^{1imag} \end{bmatrix} =$$

$$\begin{bmatrix} -\frac{1}{RC_0} & -\frac{4\sin\pi(\mathbb{D}\pi)}{\pi C_0} & -\frac{4\cos\pi(\mathbb{D}\pi)}{\pi C_0} & 0 & 0 & 0 \\ \frac{2\sin\pi(\mathbb{D}\pi)}{\pi L_{tf}} & -\frac{R_{tf}}{L_{tf}} & \omega_s & 0 & 0 & 0 \\ \frac{2\cos\pi(\mathbb{D}\pi)}{\pi L_{tf}} & -\omega_s & -\frac{R_{tf}}{L_{tf}} & 0 & 0 & 0 \\ 0 & 0 & 0 & -\frac{R_{tf}}{L_{tf}} & \frac{4\sin\pi(\mathbb{D}\pi)}{\pi L_{tf}} & \frac{4\cos\pi(\mathbb{D}\pi)}{\pi L_{tf}} \\ 0 & 0 & 0 & -\frac{2\sin\pi(\mathbb{D}\pi)}{\pi C_0} & -\frac{1}{RC_0} & \omega_s \\ 0 & 0 & 0 & -\frac{2\cos\pi(\mathbb{D}\pi)}{\pi C_0} & \omega_s & -\frac{1}{RC_0} \end{bmatrix} \times \begin{bmatrix} \triangle U_o \\ \triangle i_L^{1real} \\ \triangle i_L^{1imag} \end{bmatrix} + \begin{bmatrix} 0 & \frac{1}{C_0} \\ 0 & 0 \\ -\frac{2}{\pi L_{tf}} & 0 \end{bmatrix} \times \begin{bmatrix} U_{dc} \\ i_L \end{bmatrix} \tag{32}$$

$$\frac{d}{dt}\begin{bmatrix} \triangle U_0 \\ \triangle i_L^{1real} \\ \triangle i_L^{1imag} \end{bmatrix} = \begin{bmatrix} -\frac{1}{RC_0} & -\frac{4\sin(\mathbb{D}\pi)}{\pi C_0} & -\frac{4\cos(\mathbb{D}\pi)}{\pi C_0} \\ \frac{2\sin(\mathbb{D}\pi)}{\pi L_{tf}} & -\frac{R_{tf}}{L_{tf}} & \omega_s \\ \frac{2\cos(\mathbb{D}\pi)}{\pi L_{tf}} & -\omega_s & -\frac{R_{tf}}{L_{tf}} \end{bmatrix} \times \begin{bmatrix} \triangle U_0 \\ \triangle i_L^{1real} \\ \triangle i_L^{1imag} \end{bmatrix} + \begin{bmatrix} 0 & -\frac{1}{C_0} \\ 0 & 0 \\ -\frac{2}{\pi L_{tf}} & 0 \end{bmatrix} \times \begin{bmatrix} U_{dc} \\ i_L \end{bmatrix} \tag{33}$$

A small signal control for the output transfer function is needed to measure the system stability of the DAB converter with the controller structure. Thus, a small deviation in $\mathfrak{D}$ causes a distinction in the values of U_o^0 from its steady-state value. Hence, the corresponding small signal model is defined in Equations (34)–(37). In addition, the nonlinearity of the system is introduced when the control and state variables are multiplied. The approximation solution of nonlinear terms is presented in Equation (38). To this end, given the value of parameters defined in Equations (34)–(37) are placed into Equation (33), then the state–space model can be expressed as in Equation (39) while the corresponding values are given in A, B, C, and D matrix form. Further, the transfer function of the DAB converter can be expressed using a conversion formula, which is given in Equation (40), and the values are assigned and given in Equation (41), where $G_{open-loop}$ is the open-loop transfer function of the DAB.

$$\triangle\mathfrak{D} = \mathfrak{D} - d \tag{34}$$

$$\triangle U_o^0 = U_o^0 - U_o^0 \tag{35}$$

$$\triangle i_L^{1real} = i_L^{1real} - I_L^{1real} \tag{36}$$

$$\triangle i_L^{1imag} = i_L^{1imag} - I_L^{1imag} \tag{37}$$

$$\begin{aligned} in(\pi\mathfrak{D})U_o^0 &= \sin(\pi\mathfrak{D}) \triangle U_o^0 + U_o^0\sin(\pi\mathfrak{D})\cos(\pi \triangle \mathfrak{D}) + U_o^0\cos(\pi\mathbb{D})\sin(\pi \triangle \mathfrak{D}) \\ &= \sin(\pi\mathfrak{D}) \triangle U_o^0 + U_o^0\sin(\pi\mathfrak{D}) + U_o^0\cos(\pi\mathfrak{D}) \end{aligned} \tag{38}$$

$$\begin{aligned} \frac{d}{dt}\begin{bmatrix} \triangle U_0 \\ \triangle i_L^{1real} \\ \triangle i_L^{1imag} \end{bmatrix} &= \begin{bmatrix} -\frac{1}{RC_0} & -\frac{4\sin(\mathfrak{D}\pi)}{\pi C_0} & -\frac{4\cos(\mathfrak{D}\pi)}{\pi C_0} \\ \frac{2\sin(\mathfrak{D}\pi)}{\pi L_{tf}} & -\frac{R_{tf}}{L_{tf}} & \omega_s \\ \frac{2\cos(\mathfrak{D}\pi)}{\pi L_{tf}} & -\omega_s & -\frac{R_{tf}}{L_{tf}} \end{bmatrix} \times \begin{bmatrix} \triangle U_0 \\ \triangle i_L^{1real} \\ \triangle i_L^{1imag} \end{bmatrix} \\ &+ \begin{bmatrix} \frac{4}{C_0}\left(I_{0imag}\sin(\pi d) - I_{0real}\cos(\pi d)\right) \\ \frac{2<U_0>_o}{L_{tf}}\cos(\pi d) \\ -\frac{2<U_0>_o}{L_{tf}}\sin(\pi d) \end{bmatrix} \times \triangle\mathfrak{D} \end{aligned} \tag{39}$$

$$A = \begin{bmatrix} -178 & -363.7827 & 2.227 \times 10^{-14} \\ 1.8346 \times 10^{5} & -4.611 \times 10^{4} & 1.256 \times 10^{5} \\ 1.1234 \times 10^{-11} & -1.256 \times 10^{5} & -4.611 \times 10^{4} \end{bmatrix}_{3\times3}$$

$$B = \begin{bmatrix} 4.5 \times 10^{3} \\ 7.0585 \times 10^{-9} \\ -1.1527 \times 10^{8} \end{bmatrix}_{3\times1}$$

$$C = [1\ 0\ 0]_{1\times3} D = [0]_{1\times1}$$

$$G_{open-loop} = \left[C(sI - A)^{-1}B + D\right] \tag{40}$$

$$G_{open-loop} = \frac{4.5 \times 10^{4}s^{2} + 4.15 \times 10^{9}s + 6.072 \times 10^{15}}{s^{3} + 92398s^{2} + 1.798 \times 10^{10}s + 6.264 \times 10^{12}} \tag{41}$$

3.3. Output (DC-AC) Stage

The DC-AC stage architecture and the equivalent diagram are presented in Figure 6a and Figure 6b, respectively. Based on Figure 6b, the KVL is applied and can be expressed as Equation (42), followed by Equations (43) and (44). Further, the voltage across the capacitor and current through the load and capacitor are presented in Equation (45), Equation (46) and Equation (47), respectively. Equation (48) denotes the inverter output. Thereafter, a small signal change was applied to Equation (44), Equations (49), and (50) are obtained. Then, applying the Laplace transform to Equation (50) yields Equation (51), and the ratio is presented in Equation (52). In order to smoothen the output signal, a filter circuit is added, which is formulated in Equation (53), and the final equation is given in Equation (54). Further, using Equations (52) and (54), the obtained equations are Equations (55) and (56). Equation (57) represents the closed-loop transfer function of the output (DC-AC) stage converter. However, this closed-loop transfer function is designed without a controller. Thus, to design a controller with this transfer function, MATLAB SISOTOOL is used, and the final transfer function becomes Equation (58). Subsequently, the state–space parameters are found using Equation (58), and then controllability and observability are tested in Section 4.

$$U_{inv}(t)u(t) - L_{ac}\frac{di_{ac}(t)}{dt} - U_{c}(t) = 0 \tag{42}$$

$$L_{ac}\frac{di_{ac}(t)}{dt} = U_{inv}(t)u(t) - U_{c}(t) \tag{43}$$

where

$$u(t) = \begin{cases} 1, & U_{inv} = U_{0} \\ 0, & U_{inv} = 0 \\ -1, & U_{inv} = -U_{0} \end{cases}$$

$$L_{ac}\frac{di_{ac}}{dt} = U_{0}(t) - U_{c}(t) \tag{44}$$

$$U_{c}(t) = \frac{1}{C_{ac}}\int i_{C}(t)dt \tag{45}$$

$$i_{C}(t) = i_{ac}(t) - i_{load}(t) \tag{46}$$

$$i_{load}(t) = \frac{U_{load}}{Z} \tag{47}$$

$$U_{inv}(t)u(t) = U_{0}(t) = \mathbb{D}_{2}(t)U_{out} \tag{48}$$

$$L_{ac}\frac{d(i_{ac} + \triangle i_{ac})}{dt} = (U_{0}(t) + \triangle U_{0}(t)) - (U_{C}(t) + \triangle U_{C}(t)) \tag{49}$$

$$L_{ac}\frac{d(\triangle i_{ac})}{dt} = (\triangle U_{0}(t)) - (\triangle U_{C}(t)) \tag{50}$$

$$sL_{ac}(\triangle i_{ac}) = \triangle U_0(s) - \triangle U_C(s) \tag{51}$$

$$\frac{\triangle U_0(s)}{\triangle U_C(s)} = 1 + \frac{s^2 L_{ac} C_{ac} \triangle i_{ac}(s)}{\triangle i_C(s)} \tag{52}$$

$$\triangle i_{ac}(s) = \triangle i_C(s) + \triangle i_{Load}(s) = \triangle i_C(s) + \frac{\triangle U_C(s)}{Z} \tag{53}$$

$$\frac{\triangle i_{ac}(s)}{\triangle i_C(s)} = 1 + \frac{1}{sC_{ac}Z} \tag{54}$$

$$\frac{\triangle U_0(s)}{\triangle U_C(s)} = 1 + s^2 L_{ac} C_{ac} + \frac{sL_{ac}}{Z} \tag{55}$$

$$\text{Thus, } \frac{\triangle i_C(s)}{\triangle U_C(s)} = \frac{sC_{ac}}{1 + s^2 L_{ac} C_{ac} + \frac{sL_{ac}}{Z}} \tag{56}$$

$$G_{op} = \frac{0.00312s}{3.9 \times 10^{-9} s^2 + 8.113 \times 10^{-4} s + 1} \tag{57}$$

$$G_{op(Con)} = \frac{0.1647s}{3.047 \times 10^{-14} s^3 + 6.338 \times 10^{-9} s^2 + 4.195 \times 10^{-4} s} \tag{58}$$

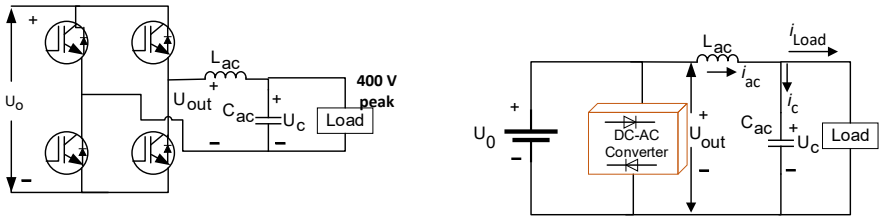

Figure 6. (**a**) DC-AC stage architecture (**b**) Equivalent diagram of DC–AC stage.

The state–space matrix of the above-mentioned equation is given as

$$A = 1 \times 10^{10} \begin{bmatrix} -0.000 & -1.3768 & 0 \\ 0 & 0 & 0 \\ 0 & 0 & 0 \end{bmatrix}$$

$$B = \begin{bmatrix} 1 & 0 & 0 \end{bmatrix}$$

$$C = 1 \times 10^{12} \begin{bmatrix} 0 \\ 0 \\ 5.4053 \end{bmatrix}$$

$$D = [0]_{1 \times 1}$$

4. Results and Discussion

The overall model of the system is developed by concatenating the models of individual parts.

4.1. Time Domain and Frequency Domain Analysis

The proposed SST model is designed and analyzed in terms of time response, frequency response, and state–space characteristics. The time response analysis is conducted by the root locus technique, which determines the absolute stability and shows the location of poles or zeros in the s-plane. This technique also determines the physical performance of the model when the gain of the input to the plant is changed from 0 to ∞. The technique is advantageous in controller design because it is organized and saves energy and time. This

study is limited to the linearized model, and both eigen analysis and frequency domain testing are applied to the linear model. In addition, time-domain analysis is studied.

Input stage numerical study: To ensure the stable operation of the system, a controller is added through MATLAB SISIOTOOL, given in Equations (59) and (60) for G_{in} and G_{vi}, respectively. The overall closed-loop transfer function of the input stage converter is given by Equation (61).

$$PI_{in} = \frac{-\left(3.825 \times 10^{-6}s + 6.5 \times 10^{-6}\right)}{s} \tag{59}$$

$$PI_{vi} = \frac{-2.7 \times 10^{-6}s + 0.0002592}{s} \tag{60}$$

$$G_{input} = \frac{2.9 \times 10^{-6}s^2 + 1.717 \times 10^{-6}s + 1.76 \times 10^{-8}}{7.65 \times 10^{-6}s^4 + 6.5 \times 10^{-6}s^3 + 6.69 \times 10^{-6}s^2 + 1.717 \times 10^{-6}s + 1.76 \times 10^{-8}} \tag{61}$$

$$A = \begin{bmatrix} -0.8497 & -0.8745 & 0.2244 & -0.0023 \\ 1 & 0 & 0 & 0 \\ 0 & 1 & 0 & 0 \\ 0 & 0 & 1 & 0 \end{bmatrix}$$

$$B = \begin{bmatrix} 1 \\ 0 \\ 0 \\ 0 \end{bmatrix}$$

$$C = \begin{bmatrix} 0 & 0.3791 & 0.2244 & 0.0023 \end{bmatrix}$$

$$D = \begin{bmatrix} 0 \end{bmatrix}$$

Input stage controllability and observability test: To test the system controllability and observability, the controllable matrix (M_c) and observable matrix (M_0) can be measured, which are expressed in Equation (62) and Equation (63), respectively, while their corresponding values are given below. Given the matrices M_c and M_0, the ranks of both are 4, which signifies the system is controllable and observable because the ranks of matrics (M_c and M_0) are the same as 4.

$$M_c = \begin{bmatrix} B & AB & A^2B & A^3B \end{bmatrix} \tag{62}$$

$$M_0 = \begin{bmatrix} C \\ CA \\ CA^2 \\ CA^3 \end{bmatrix} \tag{63}$$

$$M_c = \begin{bmatrix} 1 & -0.8497 & -0.1526 & 0.6482 \\ 0 & 1 & -0.8497 & -0.1526 \\ 0 & 0 & 1 & -0.8497 \\ 0 & 0 & 0 & 1 \end{bmatrix}$$

$$M_0 = \begin{bmatrix} 0 & 0.3791 & 0.2244 & 0.0023 \\ 0.3791 & 0.2244 & 0.0023 & 0 \\ -0.0977 & -0.3292 & -0.0851 & -0.0009 \\ -0.2462 & 0.0003 & 0.0210 & 0.0002 \end{bmatrix}$$

Isolation stage controllability and observability test: To test the system controllability and observability, the controllable and observable matrices as $\mathbf{M_c}$ and $\mathbf{M_0}$ respectively, and the values are given below.

$$M_0 = 1 \times 10^7 \begin{bmatrix} 0.0000 & 0 & 0 \\ -0.0000 & -0.0000 & 0.0000 \\ -6.6707 & 1.6839 & -4.5691 \end{bmatrix}_{3\times3}$$

$$M_c = 1 \times 10^{18} \begin{bmatrix} 0.0000 & -0.0000 & 0.0053 \\ 0.0000 & -0.0000 & 1.3348 \\ -0.0000 & 0.0000 & 1.5723 \end{bmatrix}_{3\times3}$$

From the M_c and M_0, the ranks of both are 3, which signifies the system is controllable and observable. To ensure the stability of the system and its closed-loop function, a feedback controller and a filter circuit must be added, which is expressed in Equation (64). The corresponding state–space parameters (A, B, C, and D) followed by the test matrix (controllable and observable matrix) of the isolation stage are shown below, which is also controllable and observable because the rank of the matrix is the same as that of the test matrix. Further, the closed-loop transfer function of the proposed DAB converter is expressed in Equation (65) and after the assigned value, it is presented in Equation (66).

$$G_{filter} = \frac{0.001362s + 1}{4.916 \times 10^6 s^2 + 0.04229s} \tag{64}$$

The corresponding A, B, C, and D matrix are:

$$A = 1 \times 10^3 \begin{bmatrix} -8.851 & 0 \\ 0.0010 & 0 \end{bmatrix}_{2\times2} B = \begin{bmatrix} 1 \\ 0 \end{bmatrix} C = 1 \times 10^5 \begin{bmatrix} 0.0028 & 2.0300 \end{bmatrix} D = [0]$$

$$M_c = 1 \times 10^3 \begin{bmatrix} 0.0010 & -8.5851 \\ 0 & 0.0010 \end{bmatrix} M_o = 1 \times 10^6 \begin{bmatrix} 0.0003 & 0.2030 \\ -2.1707 & 0 \end{bmatrix}$$

$$G_{closed-loop} = G_{converter} \times G_{filter} \tag{65}$$

$$G_{closed-loop} = \frac{61.29s^3 + 5.697 \times 10^6 s^2 + 8.275 \times 10^{12} s + 6.072 \times 10^{15}}{4.926 \times 10^{-6} s^5 + 0.4974s^4 + 9.25 \times 10^4 s^3 + 7.914 \times 10^8 s^2 + 2.649 \times 10^{11} s} \tag{66}$$

Output stage controllability and observability test: This sub-section is similar to Sections 3.1 and 3.2. As in Equations (62) and (63), $\mathbf{M_c}$ and $\mathbf{M_0}$ are controllable and observable matrices, and the values are given below. The ranks of these matrices are 3, which signifies the system is controllable and observable, which subsequently means that the output stage is controllable and observable.

$$\mathbf{M_c = 1 \times 10^{10}} \begin{bmatrix} \mathbf{0} & \mathbf{-0.000} & \mathbf{2.950} \\ \mathbf{0} & \mathbf{0} & \mathbf{-0.000} \\ \mathbf{0} & \mathbf{0} & \mathbf{0} \end{bmatrix}$$

$$\mathbf{M_0 = 1 \times 10^{22}} \begin{bmatrix} \mathbf{0} & \mathbf{0} & \mathbf{0} \\ \mathbf{-0.000} & \mathbf{0} & \mathbf{0} \\ \mathbf{-0.0001} & \mathbf{-7.4418} & \mathbf{0} \end{bmatrix}$$

The stability criterion is shown in Table 1. Further, the performance index is measured through frequency domain analysis and presented in Table 2 for the input, isolation, and output stages.

Table 1. Frequency response indices criteria.

Parameter	System
GM = +ve, PM = +ve	Stable
GM = −ve, PM = +ve	Unstable
GM = +ve, PM = −ve	Unstable

The frequency and time domain analysis collectively offers a better understanding of the SST behavior. The designer can recognize the critical points and stability margins to ensure reliable operation and robust performance. For instance, in the bode plot, the

response of SST, on account of the diverse frequency ranges, identifies the resonance points to ensure the system's stability. Similarly, the root locus plot is exhibited here, which can visualize the pole's movement in the system, which explains how a control parameter can change the system's stability. The Bode diagram reflects the variation in magnitude and phase with respect to frequency level at a log scale. Various parameters, such as GM, PM, ωcg, and ωcp, can be measured from the Bode plot. Thus, system stability margins can be determined. The Nyquist plot reflects the relationship between the imaginary part of the closed-loop transfer function and the radial frequency (ω) in the real axis with the variation in 'ω' from zero to infinite in the polar coordinate. This plot determines the absolute and relative stability even if the system has delays in practical assumption. The plot also provides information such as GM, PM, BW, f_{peak}, and g_{peak}. The Nichols plot is the extension of the polar plot. In this plot, magnitude and phase-angle loci at log scale versus phase diagram are in the imaginary and real axes. The location of poles and zeros of the system is presented in the pole-zero plot, and the eigenvalue of each converter in the form of a graph is depicted in Figures 7–9 for the input, isolation, and output stages, respectively. Through the use of these methods, the SST's design can be optimized for modern power distribution system applications, where stability is the main concern.

Table 2. Frequency response indices of the input stage.

Parameter	Input Stage	Isolation Stage	Output Stage
GM	Inf	Inf	Inf
PM	80.0634	5.1306	5.1306
ω_{cg}	Inf	Inf	Inf
ω_{cp}	0.8153	2.3237×10^6	2.3237×10^6
dbdrop	-3.5	-3.5	-3.5
BW	1.0110	335.0966	-1.152×10^6
K_{DC}	1	0	335.0966
f_{peak}	0.7069	33.5	0
g_{peak}	1.0534	335.0966	33.5

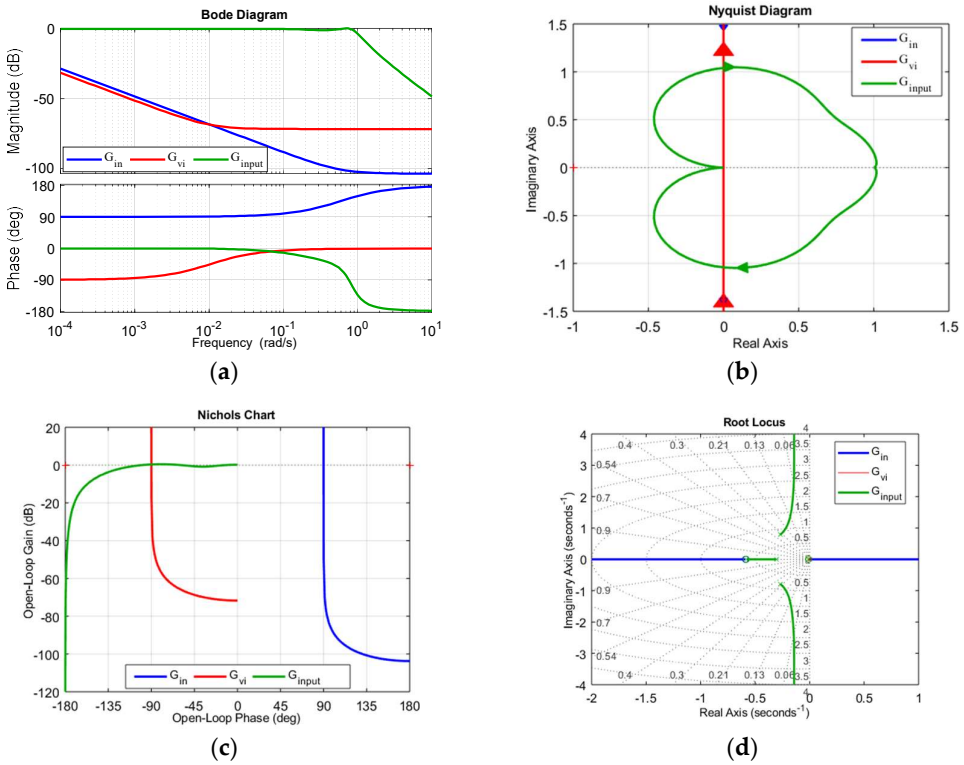

Figure 7. *Cont.*

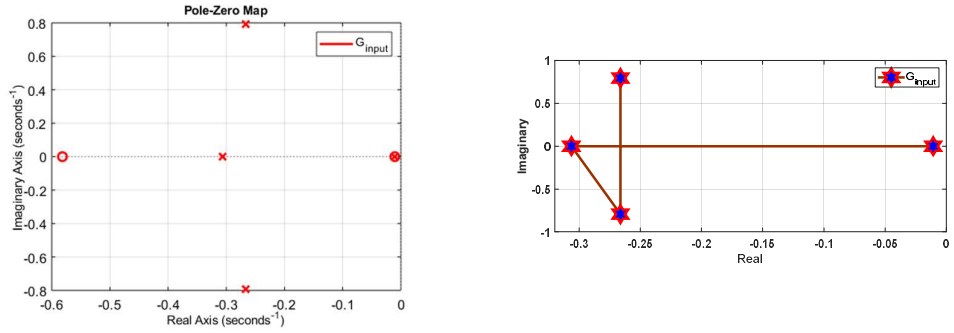

Figure 7. Input stage: (**a**) Bode plot, (**b**) Nyquist plot, (**c**) Nichols plot, (**d**) Root locus, (**e**) Pole–zero plot, (**f**) Eigen plot.

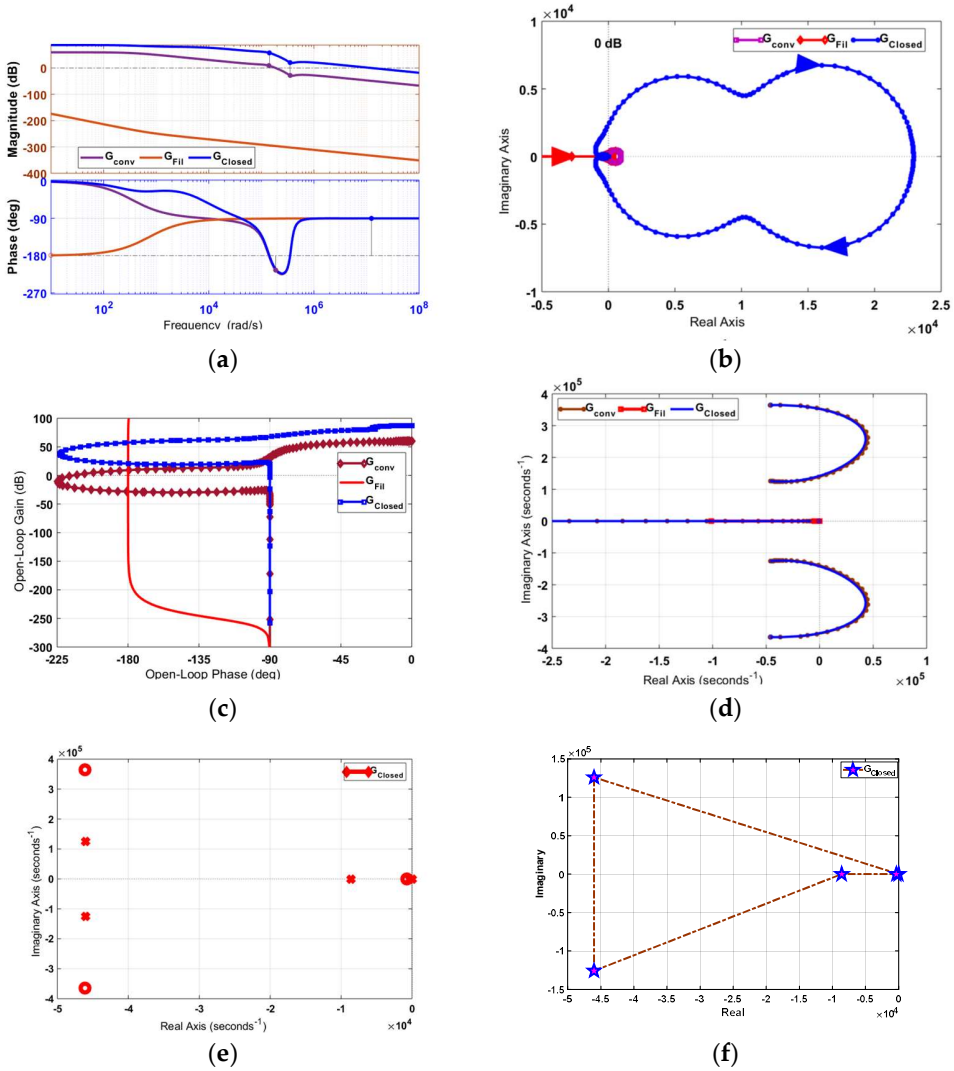

Figure 8. Isolation stage (**a**) Bode plot, (**b**) Nyquist plot, (**c**) Nichols plot, (**d**) Root locus, (**e**) Pole–zero plot, (**f**) Eigen plot.

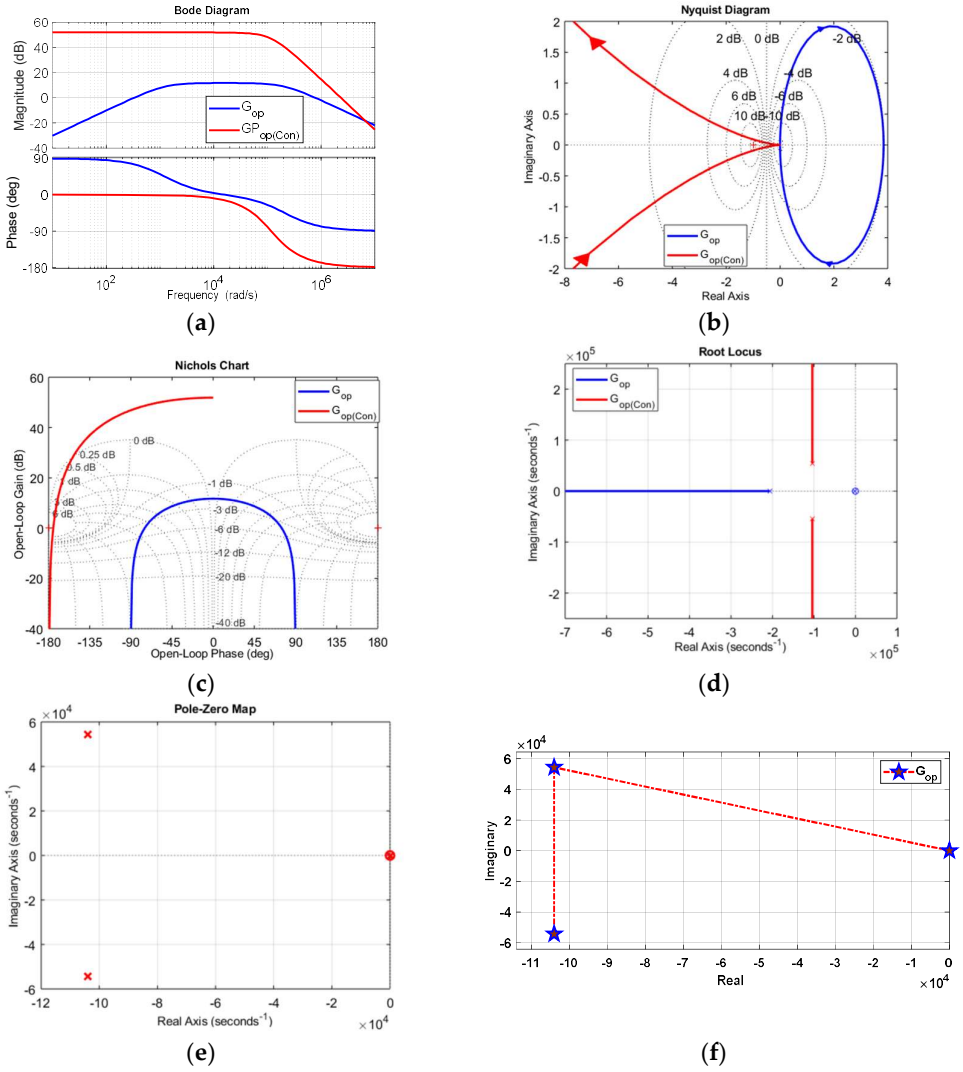

Figure 9. Output stage (**a**) Bode plot, (**b**) Nyquist plot, (**c**) Nichols plot, (**d**) Root locus, (**e**) Pole–zero plot, (**f**) Eigen plot.

4.2. Simulation Results Analysis

In this section, the simulation results of the three-stage SST are shown. The source voltage, source current, load voltage, load current, and DC-link voltage after completion of SST simulation are shown in Figure 10. The behavior of the input remains the same, even if the load side transient is disturbed. Thus, SST provides excellent isolation through the DAB converter and maintains the same phase angle at the input stage.

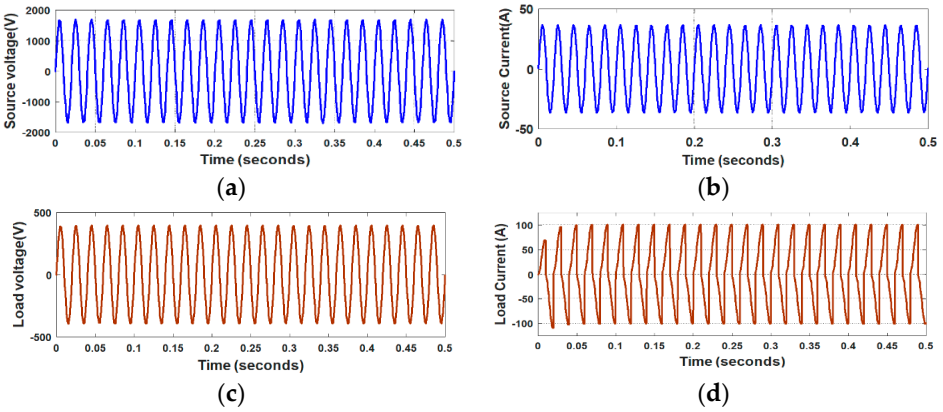

Figure 10. *Cont.*

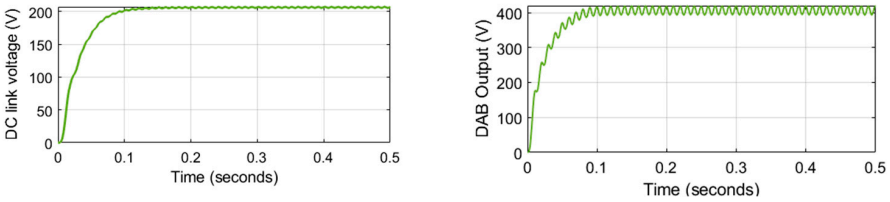

(**e**) (**f**)

Figure 10. (**a**) Source voltage. (**b**) Source current, (**c**) Load voltage (**d**) Load current, (**e**) DC-link voltage, (**f**) DAB output voltage.

4.3. Real-Time Digital Simulation

Furthermore, the Simulink model of SST has been built and executed in real-time simulation using the OPAL-RT simulator. The specification of the real-time digital simulator is OP5707XG, Intel® Xeon® processing cores with the power of a Xilinx® Virtex®-7 FPGA. The RT lab 2020 is installed on our laptop with a specification of 13th Gen Intel(R) Core(TM) i7-1355U 1.70 GHz, 64-bit operating system.

This key action marks a major advancement in the pursuit of accuracy and real-world application. The incorporation of OPAL-RT as real-time simulation is crucial and often employed for system development, analysis, and validation prior to the physical implementation. The proposed SST model has been developed using OPAL-RT software synchronization, creating an environment closely resembling real-world situations.

Figure 11 represents the real-time synchronization setup, where the SST model has been developed using RT Lab (Figure 11a), synchronized through the OPAL-RT simulator (Figure 11b), and the output can be observed on an oscilloscope (Figure 11c). Furthermore, the performance of the real-time digital model of SST is presented in Figure 12. The input voltage and current are displayed in Figure 12a,b, while the output voltage and current are shown in Figures 12c and 12d, respectively. The DAB output can be observed in Figure 12e. Based on the results, it can be concluded that it exhibits the exact performance of the Simulink model, as presented in Figure 10. The implementation of the proposed SST Simulink model with OPAL-RT for real-time simulation has been successfully validated, representing a significant accomplishment in our research and development work. This makes the proposed SST model more credible and ensures that our considerations are not limited to the virtual world but have relevance to the complexities of the actual world.

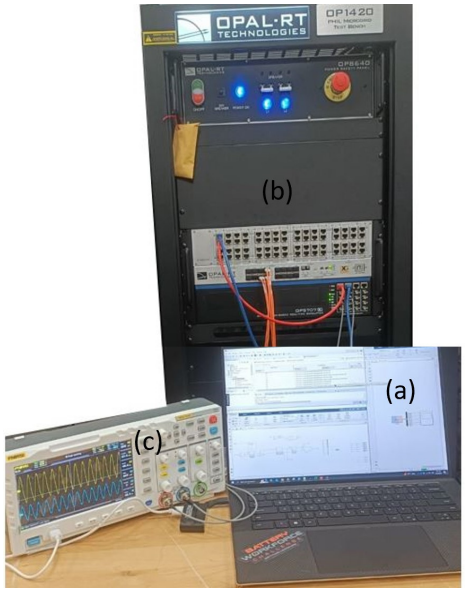

Figure 11. Real-time digital simulation setup for SST model validation. SST model has been developed using RT Lab (**a**), synchronized through the OPAL-RT simulator (**b**), and the output can be observed on an oscilloscope (**c**).

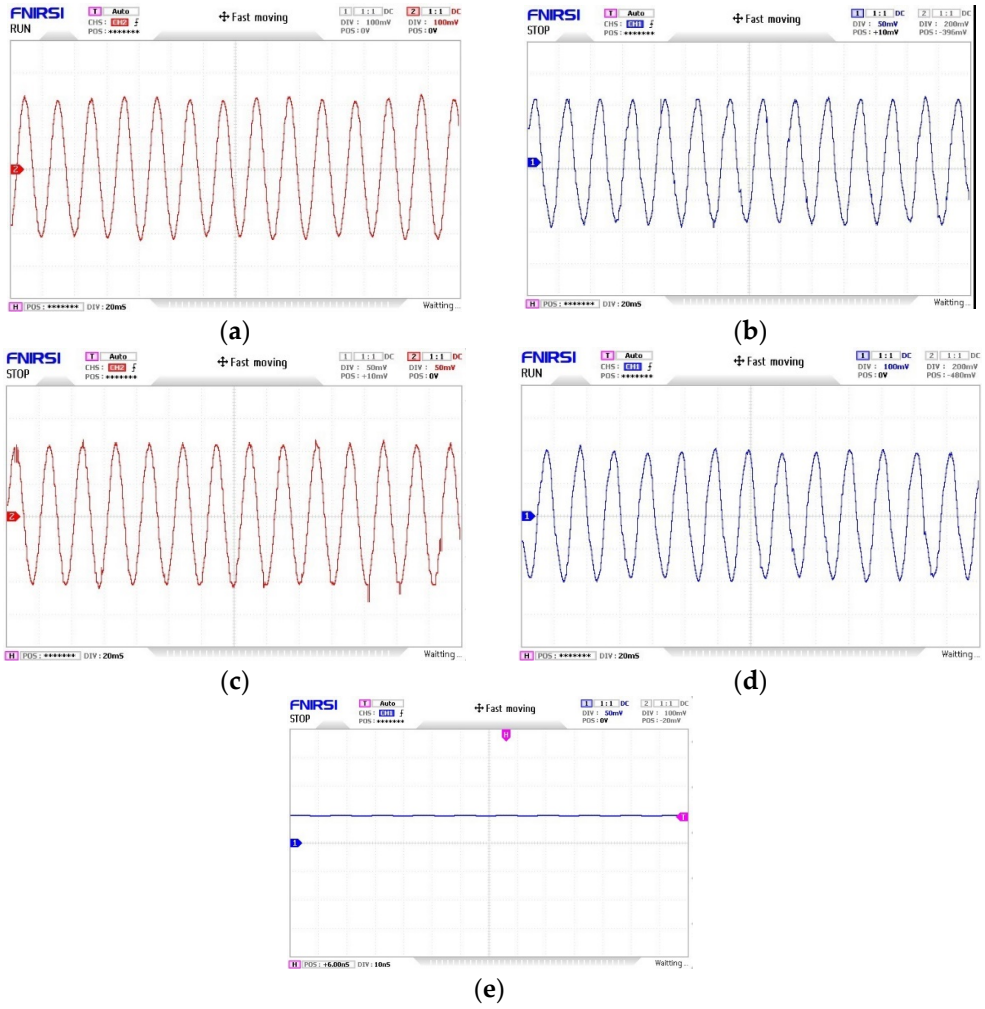

Figure 12. Real-time validation results: (**a**) Source voltage. (**b**) Source current, (**c**) Load voltage (**d**) Load current, (**e**) DC-link voltage.

5. Conclusions

In this paper, a state–space model is established to measure the stability of each converter stage for determining the SST performance with and without a controller. The analysis is conducted in three phases. In an initial attempt, the state–space model of each converter is derived, and the state–space matrixes are defined. The controllability and observability states are measured to check the system's stability. Further, the frequency and time domain analyses are performed using the Bode plot, Nyquist, Nichols, and root locus plot. On the basis of these plots, the stability, DC gain, peak resonant, and eigenvalue of the system are measured. Furthermore, the proposed SST model is simulated through the Matlab SIMULINK environment, and the results are provided, validating the systems' characteristics and seen as smooth performances. Finally, the Simulink model has been validated using a real-time digital simulator, such as OPAL-RT, to show the effectiveness of the system.

This study has particularly drawn attention to the transient performance and the stability of the system, which can be analyzed using the proposed approach, such as the state–space and transfer function-based model. The studied SST model can be implemented in distribution system applications that can cope with voltage disturbance. Besides, the SST can also manage voltage fluctuation due to intermittent sources, such as solar and wind, which, in fact, are necessary for small microgrids as they depend on 100% renewables. Moreover, the SST-based distribution system has numerous advantages, such as efficient power distribution, smart-grid realization, improved voltage regulation and stability, re-

duced environmental impact as it can enable renewable energy sources, and enhanced grid flexibility and adaptability. With the use of SST, energy providers can justify their investment to the end-user by offering resilience improvement of the distribution system by reducing the potential disturbances due to uncertainties.

The research can be extended to the stability analysis of SST by incorporating renewable energy sources as a microgrid-based system from real-time application aspects. In this paper, we considered only constant load conditions; in the future, different load types will be considered with the impact from the stability point of view. In addition, the detailed state–space model of each converter stage will be analysed.

Author Contributions: Conceptualization, D.K.M. and M.H.A.; methodology, D.K.M.; software, D.K.M.; validation, D.K.M., S.P. and S.K.S.; formal analysis, D.K.M., M.E. and L.L.; investigation, D.K.M., M.E. and S.K.S.; resources, D.K.M. and J.Z.; data curation, D.K.M.; writing—original draft preparation, D.K.M. and M.E.; writing—review and editing, D.K.M., M.H.A., S.P. and J.Z.; visualization, D.K.M.; supervision, L.L. and J.Z.; project administration, D.K.M. and M.E.; funding acquisition, D.K.M., J.Z. and L.L. All authors have read and agreed to the published version of the manuscript.

Funding: This research received no external funding.

Institutional Review Board Statement: Not applicable.

Informed Consent Statement: Not applicable.

Data Availability Statement: The raw data supporting the conclusions of this article will be made available by the authors on request.

Conflicts of Interest: The authors declare no conflicts of interest.

Glossary

AC	Alternating current
BW	Bandwidth
DAB	Dual Active Bridge
DC	Direct current
$\mathbb{D}$	Duty cycle
$\mathfrak{D}$	Small deviation
GM	Gain margin
HF	High frequency
MF	Medium frequency
PWM	Pulse width modulation
PM	Phase margin
SST	Solid State Transformer
MGs	Microgrids
N	Turns ratio
Z	Load
U	Voltage
F	Frequency
L	Leakage inductance
ϕ	Phase shift
db	decibel
SGs	Smart-grids
I	Identity matrix
U_s	input voltage
U_{dc}	dc link voltage
U_m	peak ac input voltage
$U_{inv} = U_0$	inverter output voltage
U_c	voltage across the capacitor

$\mathbb{D}_1$	averaged duty cycle
$\mathbb{D}_2$	output stage duty cycle
K_m	modulation index
R	resistance at the isolation stage
$L_f / L_{tf} / L_{ac}$	Inductor at the input, isolation, and output stage
$C_f / C_o / C_{ac}$	capacitor at the input, isolation, and output stage
Ltf & Rtf	Transformer equivalent inductance and resistance
i_{ls}	input current
i_C	current through capacitor
i_{load}	load current
i_C	current through inductor at the output stage
$\triangle i_{ls}(t)$	change in input current
G_{in} and G_{vi}	current and voltage control loop transfer function of the input stage
$G_{open-loop}$	open loop transfer function of the isolation stage
G_{op} and $G_{op(con)}$	transfer function of the output stage without and with controller
G_{filter}	feedback controller for filter circuit for the output stage
$G_{closed-loop}$	closed-loop transfer function of the output stage
G_{PI1} and G_{PI1}	PI controller for G_{in} and G_{vi}
fs	switching frequency
U_0	voltage across the capacitor
i_L	current through the inductor
M_c *and* M_o	controllable and observable matrix
GM and PM	Gain and phase margin
BW	bandwidth
ω_{cg} and ω_{cg}	gain crossover and phase crossover frequency
f_{peak} and g_{peak}	peak frequency and gain peak
K_{DC}	DC gain

Appendix A

Table A1. System parameters and their value.

Input Stage	Isolation Stage	Output Stage
U_{in} = 1.2 kV rms U_{peak} = 1.7 kV L_s = 15 mH C_f = 420 µF *Modulation index* = 0.85 $\mathbb{D}_1$ = 0.5	U_{dc} = 2 kV U_0 = 400 V Switching frequency = 20 kHz C_0 = 0.0035 F L_{tf} = 0.00347 mH, R_{rf} = 0.16 Ω, R_0 = 1.6051 Ω, P_{out} = 16 kW $\mathbb{D}$ = 0.5	U_C = 40 0V L_{ac} = 1 mH C_{ac} = 7.8 µF $\mathbb{D}_2$ = 0.5

References

1. Wang, C.; Ju, P.; Wu, F.; Pan, X.; Wang, Z. A systematic review on power system resilience from the perspective of generation, network, and load. *Renew. Sustain. Energy Rev.* **2022**, *167*, 112567. [CrossRef]
2. Mishra, D.K.; Eskandari, M.; Abbasi, M.H.; Sanjeevkumar, P.; Zhang, J.; Li, L. A detailed review of power system resilience enhancement pillars. *Electr. Power Syst. Res.* **2024**, *230*, 110223. [CrossRef]
3. Guo, W.; Qureshi, N.M.F.; Jarwar, M.A.; Kim, J.; Shin, D.R. AI-Oriented Smart Power System Transient Stability: The Rationality, Applications, Challenges and Future Opportunities. *Sustain. Energy Technol. Assess.* **2023**, *56*, 102990. [CrossRef]
4. Wang, J.; Mishra, D.K.; Li, L.; Zhang, J. Demand Side Management and Peer-to-Peer Energy Trading for Industrial Users Using Two-Level Multi-Agent Reinforcement Learning. *IEEE Trans. Energy Mark. Policy Regul.* **2023**, *1*, 23–36. [CrossRef]
5. Shaukat, N.; Islam, M.R.; Rahman, M.M.; Khan, B.; Ullah, B.; Ali, S.; Fekih, A. Decentralized, Democratized, and Decarbonized Future Electric Power Distribution Grids: A Survey on the Paradigm Shift from the Conventional Power System to Micro Grid Structures. *IEEE Access* **2023**, *11*, 60957–60987. [CrossRef]
6. Du, P.; Baldick, R.; Tuohy, A. Integration of large-scale renewable energy into bulk power systems. *Power Electron. Power Syst.* **2017**, *10*, 973–978.
7. Naebi, A.; SeyedShenava, S.; Contreras, J.; Ruiz, C.; Akbarimajd, A. EPEC approach for finding optimal day-ahead bidding strategy equilibria of multi-microgrids in active distribution networks. *Int. J. Electr. Power Energy Syst.* **2020**, *117*, 105702. [CrossRef]

8. Chen, J.; Mohamed, M.A.; Dampage, U.; Rezaei, M.; Salmen, S.H.; Obaid, S.A.; Annuk, A. A multi-layer security scheme for mitigating smart grid vulnerability against faults and cyber-attacks. *Appl. Sci.* **2021**, *11*, 9972. [CrossRef]
9. Wu, X.; Wang, Z.; Ding, T.; Wang, X.; Li, Z.; Li, F. Microgrid planning considering the resilience against contingencies. *IET Gener. Transm. Distrib.* **2019**, *13*, 3534–3548. [CrossRef]
10. Hossein Abbasi, M.; Taki, M.; Rajabi, A.; Li, L.; Zhang, J. Risk-constrained offering strategies for a large-scale price-maker electric vehicle demand aggregator. *IET Smart Grid* **2020**, *3*, 860–869. [CrossRef]
11. Mishra, D.K.; Wang, J.; Li, L.; Zhang, J.; Hossain, M. Resilience-Driven Scheme in Multiple Microgrids with Secure Transactive Energy System Framework. *IEEE Trans. Ind. Appl.* **2023**. [CrossRef]
12. Alotaibi, I.; Abido, M.A.; Khalid, M.; Savkin, A.V. A comprehensive review of recent advances in smart grids: A sustainable future with renewable energy resources. *Energies* **2020**, *13*, 6269. [CrossRef]
13. Kerdphol, T.; Ngamroo, I.; Surinkaew, T. Enhanced robust frequency stabilization of a microgrid against simultaneous cyber-attacks. *Electr. Power Syst. Res.* **2024**, *228*, 110006. [CrossRef]
14. Rokrok, E.; Shafie-Khah, M.; Catalao, J.P. Review of primary voltage and frequency control methods for inverter-based islanded microgrids with distributed generation. *Renew. Sustain. Energy Rev.* **2018**, *82*, 3225–3235. [CrossRef]
15. Gorjian, A.; Eskandari, M.; Moradi, M.H. Conservation Voltage Reduction in Modern Power Systems: Applications, Implementation, Quantification, and AI-Assisted Techniques. *Energies* **2023**, *16*, 2502. [CrossRef]
16. Atkar, D.D.; Chaturvedi, P.; Suryawanshi, H.M.; Nachankar, P.P.; Yadeo, D. Optimal Design of Solid State Transformer-Based Interlink Converter for Hybrid AC/DC Micro-Grid Applications. *IEEE J. Emerg. Sel. Top. Power Electron.* **2021**, *10*, 3685–3696. [CrossRef]
17. She, X.; Yu, X.; Wang, F.; Huang, A.Q. Design and demonstration of a 3.6-kV–120-V/10-kVA solid-state transformer for smart grid application. *IEEE Trans. Power Electron.* **2013**, *29*, 3982–3996. [CrossRef]
18. Ortiz, G.; Uemura, H.; Bortis, D.; Kolar, J.W.; Apeldoorn, O. Modeling of soft-switching losses of IGBTs in high-power high-efficiency dual-active-bridge DC/DC converters. *IEEE Trans. Electron Devices* **2012**, *60*, 587–597. [CrossRef]
19. Zhao, T.; Zeng, J.; Bhattacharya, S.; Baran, M.E.; Huang, A.Q. An average model of solid state transformer for dynamic system simulation. In Proceedings of the 2009 IEEE Power & Energy Society General Meeting, Calgary, AL, Canada, 26–30 July 2009; pp. 1–8.
20. Shah, D.G.; Crow, M. Stability design criteria for distribution systems with solid-state transformers. *IEEE Trans. Power Deliv.* **2014**, *29*, 1–8. [CrossRef]
21. Wang, Z.; Xu, J.; Hatua, K.; Madhusoodhanan, S.; Bhattacharya, S. Solid state transformer specification via feeder modeling and simulation. In Proceedings of the 2012 IEEE Power and Energy Society General Meeting, San Diego, CA, USA, 22–26 July 2012; pp. 1–5.
22. Zhu, Q. *7.2 kV Solid State Transformer Based on 15 kV SiC MOSFETs and A Novel Single Stage AC-AC Converter*; North Carolina State University: Charlotte, CA, USA, 2017.
23. Lai, J.-S.; Lai, W.-H.; Moon, S.-R.; Zhang, L.; Maitra, A. A 15-kV class intelligent universal transformer for utility applications. In Proceedings of the 2016 IEEE Applied Power Electronics Conference and Exposition (APEC), Long Beach, CA, USA, 20–24 March 2016; pp. 1974–1981.
24. Motwani, J.K.; Liu, J.; Boroyevich, D.; Burgos, R.; Zhou, Z.; Dong, D. Modeling and Control of a Hybrid Modular Multilevel Converter for High-AC/Low-DC Medium-Voltage Applications. *IEEE Trans. Power Electron.* **2024**, *4*, 265–282. [CrossRef]
25. Wang, G.; Baek, S.; Elliott, J.; Kadavelugu, A.; Wang, F.; She, X.; Dutta, S.; Liu, Y.; Zhao, T.; Yao, W. Design and hardware implementation of Gen-1 silicon based solid state transformer. In Proceedings of the 2011 Twenty-Sixth Annual IEEE Applied Power Electronics Conference and Exposition (APEC), Fort Worth, TX, USA, 6–11 March 2011; pp. 1344–1349.
26. Kim, S.-H.; Jang, Y.-H.; Kim, R.-Y. Modeling and Hierarchical Structure Based Model Predictive Control of Cascaded Flying Capacitor Bridge Multilevel Converter for Active Front-End Rectifier in Solid-State Transformer. *IEEE Trans. Ind. Electron.* **2018**, *66*, 6560–6569. [CrossRef]
27. Khazraei, M.; Prabhala, V.A.K.; Ahmadi, R.; Ferdowsi, M. Solid-state transformer stability and control considerations. In Proceedings of the 2014 IEEE Applied Power Electronics Conference and Exposition-APEC 2014, Forth Worth, TX, USA, 16–20 March 2014; pp. 2237–2244.
28. Parimi, M.; Monika, M.; Rane, M.; Wagh, S.; Stankovic, A. Dynamic phasor-based small-signal stability analysis and control of solid state transformer. In Proceedings of the 2016 IEEE 6th International Conference on Power Systems (ICPS), New Delhi, India, 4–6 March 2016; pp. 1–6.
29. Shah, D.; Crow, M. Stability assessment extensions for single-phase distribution solid-state transformers. *IEEE Trans. Power Deliv.* **2015**, *30*, 1636–1638. [CrossRef]
30. Wang, R.; Sun, Q.; Zhang, X.; Du, Y. The Impedance-Based Stability Analysis of the Single-Phase Solid State Transformer. In Proceedings of the 2018 Chinese Automation Congress (CAC), Xi'an, China, 30 November–2 December 2018; pp. 35–40.
31. Saleh, S.A.; Richard, C.; Onge, X.F.S.; McDonald, K.M.; Ozkop, E.; Chang, L.; Alsayid, B. Solid-state transformers for distribution systems–Part I: Technology and construction. *IEEE Trans. Ind. Appl.* **2019**, *55*, 4524–4535. [CrossRef]
32. Bifaretti, S.; Zanchetta, P.; Watson, A.; Tarisciotti, L.; Clare, J.C. Advanced power electronic conversion and control system for universal and flexible power management. *IEEE Trans. Smart Grid* **2011**, *2*, 231–243. [CrossRef]

33. Qin, H.; Kimball, J.W. Solid-state transformer architecture using AC–AC dual-active-bridge converter. *IEEE Trans. Ind. Electron.* **2012**, *60*, 3720–3730. [CrossRef]
34. Jeyapradha, R.; Rajini, V. Small signal averaged transfer function model and controller design of modular solid state transformers. *ISA Trans.* **2019**, *84*, 271–282.